Journal of Membrane Science 736 (2025) 124606

Contents lists available at ScienceDirect

Journal of Membrane Science

journal homepage: www.elsevier.com/locate/memsci

Intercrystalline defect healing in polycrystalline MOF membranes by pressurized counter-diffusion secondary growth

Fatereh Dorosti [a,b], Lei Ge [b,*], Shazed Aziz [a], John Bell [b], Zhonghua Zhu [a,**]

[a] Department of Chemical Engineering, University of Queensland, Brisbane, QLD, 4072, Australia
[b] Center for Future Materials, School of Engineering, University of Southern Queensland, Springfield, QLD, 4300, Australia

ARTICLE INFO

Keywords:
Intercrystalline defects
Metal-Organic frameworks
Membranes
Recrystallization
Separation

ABSTRACT

The significance of membranes in the future of sustainable energy and emission reduction is universally recognized, as they play a crucial role in processes such as hydrogen production, decarbonization, and power generation. Molecular sieving polycrystalline MOF membranes hold considerable promise among various membrane materials due to their selective pore structures. However, the full potential of molecular sieving is compromised by the unavoidable defect formation during membrane synthesis, resulting in reduced membrane separation efficiency, stability, repeatability, and scalability. Here, we introduced a novel intercrystalline healing process utilizing pressurized counter-diffusion to address this long-lasting challenge of polycrystalline membranes and to achieve microstructure evolution and heal typical intercrystalline defects in MOF membranes. This method enables the controlled infiltration of precursors into defects for crystal growth, followed by sealing the unselective gaps through Ostwald ripening. Therefore, a compact and uniform MOF layer with significantly reduced intercrystalline defects can be formed. The final membrane demonstrates a 91 % reduction in total defect volume, while most remaining defects become isolated with less impact on the membrane selectivity. In the healed ZIF, the H_2/N_2 selectivity improved over 15-fold compared to the initial ZIF membrane, surpassing peers and achieving an optimal balance in the permeability-selectivity trade-off. Similar improvements were observed for other polycrystalline MOF membranes (e.g., CuBTC), highlighting the universality of addressing the common defect issue in various MOF and polycrystalline membranes.

1. Introduction

Membranes are a critical sustainable separation technology in the renewable energy sector and the broader decarbonization efforts. Their application spans a range of pivotal areas, including biogas upgrading to biomethane, hydrogen infrastructure such as blue hydrogen production, and carbon capture to mitigate the greenhouse gas emissions from industrial processes and power generation. By enhancing the efficiency of these processes, membranes are indispensable in advancing renewable energy solutions, achieving decarbonization goals, and contributing to the reduction of the overall environmental footprint.

Within the realm of membrane materials, Metal-Organic Frameworks (MOFs) have attracted considerable attention owing to their exceptional structural adaptability [1], selective separation properties, and facile synthesis protocols [2]. Nonetheless, the application of pure MOF membranes at industrial scales is impeded by a myriad of challenges that necessitate further investigation and resolution [3].

The primary mechanism facilitating effective separation in polycrystalline membranes relies on molecular transport through the selective pores. The presence of cracks and defects can severely compromise the selectivity of these membranes. Consequently, it appears that the currently achieved level of separation performance is limited predominantly by membrane defects rather than the inherent selectivity of the pores. Current separation properties still fall considerably short of theoretical values, and the inconsistency in membrane performance among the same materials highlights this challenge [4,5]. Moreover, the existence of defects reduces the stability of membranes, compromises their reproducibility, and poses significant challenges to their scalability [4]. Therefore, in addition to advances in material science and the introduction of new MOF materials, there is a pressing need for innovative approaches to reduce the density of defects within the membranes.

* Corresponding author.
** Corresponding author.
E-mail addresses: lei.ge@usq.edu.au (L. Ge), z.zhu@uq.edu.au (Z. Zhu).

https://doi.org/10.1016/j.memsci.2025.124606
Received 13 June 2025; Received in revised form 4 August 2025; Accepted 24 August 2025
Available online 26 August 2025

The efforts to mitigate defects in polycrystalline membranes can be categorized into two main approaches: bottom-up synthetic control and post-synthesis defect filling. The former strategy involves various techniques to establish a higher degree of control over precursor reaction speed, crystal formation, and crystal growth direction, with the ultimate objective of reducing defect density. Examples of such methods include contra-diffusion [6], secondary growth [7–10], confinement growth [11,12], and electrochemical synthesis [13]. However, these methodologies are typically non-universal and necessitate customization for specific types of MOF membranes.

On the other hand, post-synthesis defect filling entails employing diverse materials and methodologies to fill the defects after the synthesis process [14]. These methods have wider applicability and can be used with various materials, providing more flexibility and allowing for selective customization to target specific defect types. Moreover, these methods mitigate the complexity associated with primary synthetic methodologies, align well with existing membrane technologies, and are suitable for commercially available MOF membranes. Some post-synthesis modification techniques, such as polymer coating [15] or infilling defects with substances like coke have been investigated in various MOF and zeolite membranes [14,16,17]. While these materials can effectively fill defects, they may block the substrate pores, leading to a significant reduction in the active permeation area. Moreover, defects can be sealed through secondary reactions to form selective materials, either identical to the initial layer or distinct, such as filling defects with MOFs, Covalent Organic Frameworks (COFs), or using ionic liquids. In such methods, selectivity enhancement occurs for two primary reasons: filling unselective defects and introducing additional selective materials to the initial phase. However, in secondary growth techniques aimed at defect filling, precise control over the reaction site is crucial to target defect areas and prevent pore blockage or the formation of multiple layers without a reduction in defect density. So, designing new strategies and novel approaches to target the defects effectively is highly demanded. A potential solution can be employing methods such as contra-diffusion or interfacial reaction, which are prominent for their self-regulation mechanism [18,19]. Nevertheless, another challenge arises in these methods. The high capillary pressure within defects acts as a barrier, impeding precursor diffusion into these regions and preventing their crystallization within the defects. Therefore, innovative methods and engineered techniques are required to effectively address the issue of defects.

Here, we designed a novel technique to target the defect issue in polycrystalline membranes. The Pressurized Counter Diffusion Process (PCDP) has been introduced to regulate the crystal formation within the membrane intercrystalline defects and enable a microstructure evolution in MOF membranes. Applying pressure to both sides of the membrane alleviates capillary pressure within the defects, promoting the infiltration of precursor species. This facilitates defect-site recrystallization, thereby reconstructing the membrane morphology and yielding a uniform layer with sealed intercrystalline defects and enhanced performance. This study demonstrates how minor modifications and targeted engineering strategies can refine the microstructure of crystalline membranes, leading to a substantial enhancement in their performance.

2. Materials and experiments

2.1. Materials

The α-Alumina substrate with a pore size of 70 nm was purchased from Fraunhofer IKTS. The substrate was washed with ethanol and acetone several times before use. All chemicals including Ethylene glycol, Ethanolamine, 2-methylimidazole (Hmim, 99.0 %), Zinc nitrate hexahydrate ($Zn(NO_3)_2.6H_2O$ 99.99 %), Zinc acetate dihydrate ($Zn(CH_3COO)_2.2H_2O$ 99.99 %), Copper(II) nitrate trihydrate $Cu(NO_3)_2$ $3H_2O$, trimesic acid (H_3BTC), fluorescein sodium salt, anhydrous ethanol (≥99.7 %), Acetone (99.0 %), were purchased from Sigma-Aldrich and used without further purification.

2.2. Fabrication of the PCDP ZIF membrane

A schematic diagram of the fabrication process of ZIF-8 has been demonstrated in Fig. S2. A three-step procedure has been conducted to ensure the fabrication of the compact ZIF membrane with reduced defect density.

Step 1: Fabrication of zinc oxide-coated α-Alumina substrate: A solution comprising 0.3 M zinc acetate dihydrate and 0.01 M ethanolamine in ethylene glycol was prepared, undergoing a thorough mixing process at 70 °C for 2 h, yielding a slurry consisting of ZnO particles. In the next step, the α-Alumina substrates were coated with the prepared solution two times, employing spin-coating techniques at a speed of 600 rpm. Following each coating procedure, the membranes were dried at 100 °C for 1 h. The subsequent calcination process for the ZnO layer was performed at 400 °C for 2 h using a furnace.

Step 2: Fabrication of Initial ZIF membrane: The ZnO layer in the ZnO-coated substrate initiates ZIF-8 nucleation and serves as a sacrificial template/seed layer for ZIF formation. In this study, this layer is referred to as the "ZnO-seed". The transformation of the ZnO layer into a ZIF-8 layer was achieved by immersing the ZnO-coated substrate in a solution of 0.8 M Hmim in water within a 25 ml Teflon-lined stainless-steel autoclave, maintaining a temperature of 90 °C for 24 h. The autoclave was gradually cooled to room temperature, and the resultant membranes were thoroughly washed with ethanol before being dried at 60 °C.

Step 3: Fabrication of PCDP ZIF: The PCDP ZIF is fabricated utilizing the pressurized contra-diffusion method. The membranes from Step 2 were positioned at the center of a counter-diffusion cell. On one side, a solution of 0.8 M Hmim in water was introduced, while the other side was filled with a solution of 0.15 M zinc nitrate in water. The membrane surface faced the Hmim side of the cell. Both sides of the cell were connected to argon gas to apply the necessary pressure and were situated in a beads heating bath to control temperature. Equal pressure was maintained on both sides of the membrane to prevent mechanical damage from pressure gradients and to keep the reaction location stable and controllable. The modification process was conducted under various conditions (temperature, pressure, and time), as outlined in the experimental parameters detailed in the Table 1. The final membranes were washed with ethanol and subsequently dried at 60 °C.

2.3. Fabrication of the PCDP CuBTC membrane

The fabrication steps for the PCDP CuBTC membrane have been shown in Fig. S3.

Step 1: Fabrication of $Cu(OH)_2$ Modified α-Alumina Substrate: A solution comprising 0.01 M copper nitrate trihydrate and 0.01 M ethanoamine in water was continuously mixed, resulting in a distinctive blue liquid. Subsequently, 1 ml of this seeding liquid was vacuum-filtered onto a 1 cm diameter alumina substrate,

Table 1
Sample names and experimental conditions.

Sample name	Temperature °C	Pressure	Time (hr)
Initial ZIF	No Process		
SG-ZIF	Room	No Pressure	72
PCDP ZIF	Room	8 bar	72
PCDP ZIF-t	Room	8 bar	Variable (1–72)
HT-ZIF	80	8 bar	72
PCDP CuBTC	Room	8 bar	72

establishing a $Cu(OH)_2$ seed layer. The coated substrate was dried at room temperature for 1 h.

Step 2: Fabrication of Initial CuBTC membrane: The ZnO-coated substrate was immersed in a solution containing 0.01 M trimesic acid in a water/ethanol mixture (1:1) for 6 h at room temperature. This facilitated the formation of a CuBTC layer on the substrate.

Step 3: Fabrication of PCDP CuBTC: The previously fabricated membrane, originating from the prior step, was positioned within the counter diffusion cell. The surface of the membrane was exposed to a solution with a ligand concentration of 0.01 M in water/ethanol, while the metal ions side featured a concentration of 0.02 M copper nitrate trihydrate in water/ethanol. The membrane underwent modification at room temperature, subject to 8 bar pressure, persisting for 3 days on both sides of the membrane.

2.4. Characterization

Various analyses were conducted to characterize the morphology, crystallinity, and properties of the fabricated membranes.

The SEM characterization employed a JEOL JSM-7800F SEM EBSD instrument, with samples meticulously prepared on suitable holders and coated with a Pt layer. For cross-section SEM images, membranes were deliberately cracked before preparation. The membranes were fractured in a controlled manner for SEM analysis by placing a blade-like object on their surface and applying a sudden force. Although this fracturing method is useful, there is still a risk of damaging the membrane structure during the process. Therefore, for more sensitive analyses such as TEM and 3D SEM, focused ion beam (FIB) was employed to prepare high-quality cross-sections with minimal structural artifacts.

Surface roughness and topography were analyzed through AFM analysis, conducted with the Bruker MultiMode 8-HR instrument.

XRD analysis, utilizing the Rigaku SmartLab instrument, was used to study the crystallinity of membranes over an angle range of 5–60 with a 0.5°/min time per step.

FTIR analysis, conducted with a PerkinElmer Spectrum 100 instrument, delved into the chemical bonds of the membrane, while an XPS Kratos Axis Ultra photoelectron spectrometer characterized surface elements, with detailed scans for Zn 2p, C 1s, N 1s, O 1s, and Al 2p elements.

ZEISS LSM 900 upright laser scanning confocal microscopy was employed to investigate the defect distribution in various samples. A dye solution containing 0.1 M fluorescein sodium salt in water was utilized for this test. To examine the effect of pressure on driving precursors into the defects, three initial ZIF samples were placed in a pressurized counter-diffusion cell. Both sides of the cell were filled with the aforementioned dye solution. Subsequently, pressures of 0, 4, and 8 bars were applied to both sides for three days. The prepared samples were then analyzed using laser scanning confocal microscopy. Additionally, to compare the defects in PCDP ZIF and Initial ZIF membranes, both were soaked in the dye solution without pressure for three days before the confocal microscopy test.

NX5000 FIB-SEM instrument and Amira software have been used to reconstruct the 3D image of the fabricated membrane and investigate the defect density.

Transmission electron microscopy (TEM) analysis was conducted using the Hitachi HF5000 instrument to investigate the morphology of the PCDP membrane. The sample was delaminated using the NX5000 FIB instrument.

2.5. Gas permeation test

2.5.1. Single gas permeation measurement

To assess the performance of the fabricated membranes, gas permeation tests were conducted utilizing a constant volume setup, as illustrated in Fig. S4. The membranes were securely placed in the permeation cell, and the permeation of H_2 and N_2 gases was measured at room temperature and 2 bar pressure.

The permeability and selectivity of the membranes were determined using the following equation:

$$P = \frac{273.15 \times 10^{10} \times VL}{760AT \times \left(\frac{P_0 \times 76}{14.7}\right)} \times \frac{dp}{dt} \quad (1)$$

Where P is the gas permeability in barrer (1 barrer = 1 × 10-10 cm^3 (STP) cm cm^{-2} s^{-1} cm Hg^{-1}), A is the effective area of the membrane (cm^2), T is the absolute temperature (K), V is the volume of the downstream chamber (cm^3), L is the membrane thickness (cm), P0 is the feed pressure (psi), and dp/dt is the steady rate of pressure increase in the downstream side (mmHg.s^{-1}).

$$\alpha = \frac{P_A}{P_B} \quad (2)$$

Where α is the ideal selectivity of the membrane. P_A and P_B are the permeabilities of pure A and B gases, respectively. Each sample was tested twice, and the average result was reported.

2.5.2. Mixed gas permeation measurement

In order to explore the molecular interaction among gas molecules during gas transport through the membrane, a mixed gas permeation experiment was performed utilizing a gas mixture consisting of 50 % hydrogen (H_2) and 50 % nitrogen (N_2) by volume. The total permeability across the membrane was measured using the constant volume method, employing Equation (1) under a pressure of 2 bar. To analyze the composition of the gas mixture, a representative sample of the permeate gas was subjected to gas chromatography (GC) using Ar as the sweep gas. Subsequently, the selectivity and permeability of each gas were determined by employing the following equations:

$$\alpha_{ij} = \frac{\left(\frac{y_i}{y_j}\right)_{Permeate}}{\left(\frac{y_i}{y_j}\right)_{Feed}} \quad (3)$$

$$P_i = P_t \times y_i \quad (4)$$

Where α is the selectivity, y is the volume percent of each component in permeate and feed gas, Pt is the total permeability, and pi is the permeability of each component.

Two samples of the final PCDP ZIF were tested for the mixed gas test, and each sample was tested twice. The average result is reported in Table S4.

3. Results and discussion

3.1. Main findings

The schematic of the proposed PCDP is illustrated in Fig. 1a. The PCDP follows three main steps: accumulation of precursors in the defects by overcoming capillary pressure owing to the high-pressure environment, followed by the interfacial reaction of precursors within these areas, breaking the initial crystalline structure, recrystallization, and ultimately, Ostwald ripening to smooth the surface, minimize defects, and induce morphological alterations. Fig. 1b and c depict the SEM images of the membrane, representative of a typical ZIF-8 membrane, whose microstructure reflects the prior literature observation [20–23]. Upon treatment with PCDP, the membrane's microstructure undergoes reconstruction, resulting in the formation of a uniform layer characterized by sealed intercrystalline defects and the elimination of grain boundary defects, as evidenced by SEM images (Fig. 1d and e). Moreover, the transmission electron microscopy (TEM) analysis of the PCDP membrane revealed a uniform ZIF-8 layer with no visible defects,

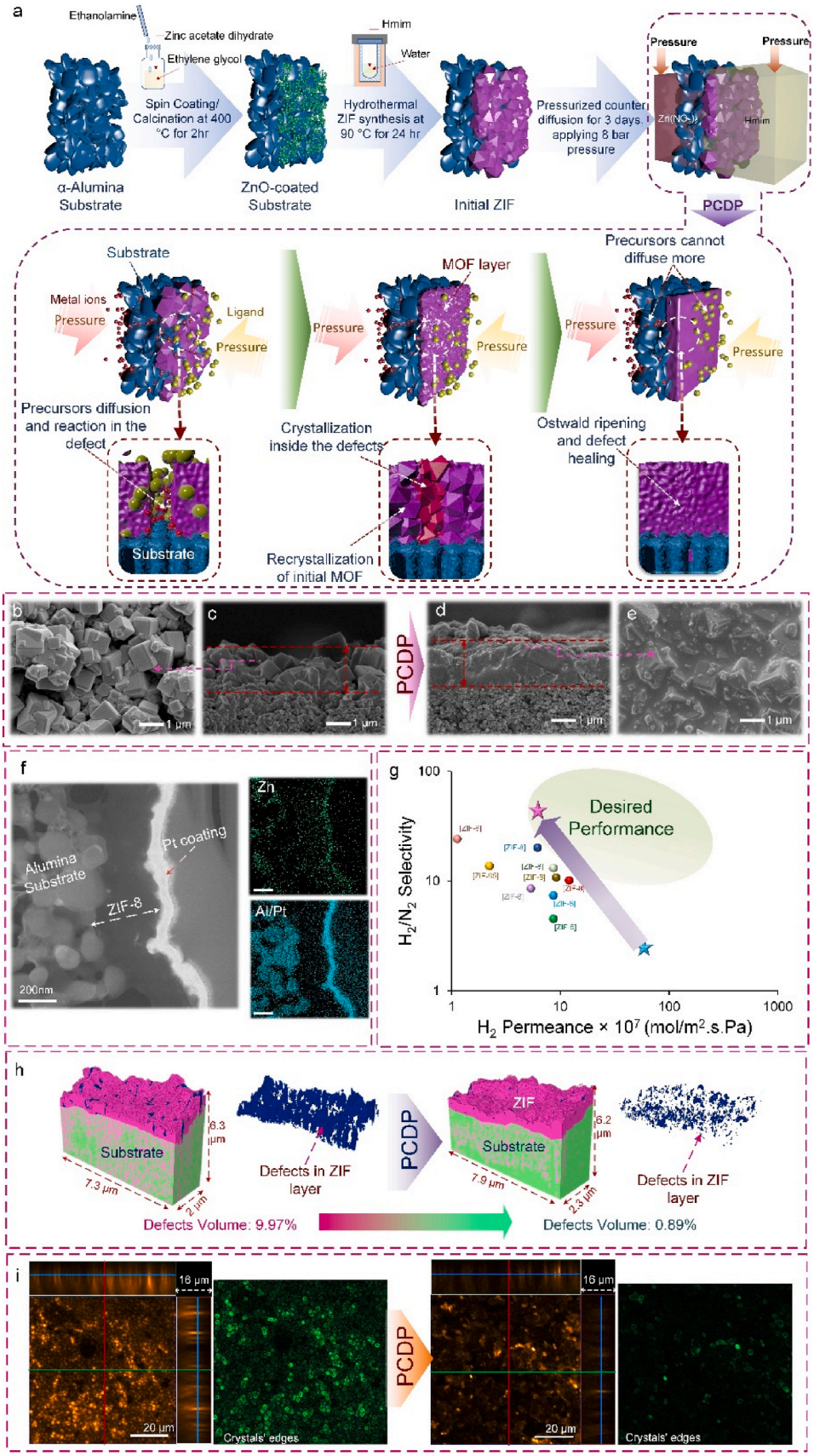

(caption on next page)

Fig. 1. Pressurized Counter Diffusion Process (PCDP), structure and performance. (a) The schematic view of the Pressurized Counter Diffusion Process, (c,d) Cross section and (b,e) Surface SEM images of membranes, (b,c) Initial ZIF, (d,e) PCDP ZIF, (f) TEM and EDX mapping of PCDP membrane, (g) H_2/N_2 separation results of the Initial and PCDP ZIF-8 membranes compared to other MOF membranes in literature [24–32]. Blue star: Initial ZIF and purple star: PCDP ZIF. (h) The FIB-SEM 3D reconstruction of the ZIF-8 membrane (Initial and PCDP samples) highlights the significant decrease in defect density. Segment color: Purple: ZIF crystals, Green: substrate, and Dark blue: defects. (i) Fluorescent Confocal Optical Microscopy (FCOM) test results, Initial and PCDP ZIF. Image with green lights: processed surface image using the "find edge" method. (For interpretation of the references to color in this figure legend, the reader is referred to the Web version of this article.)

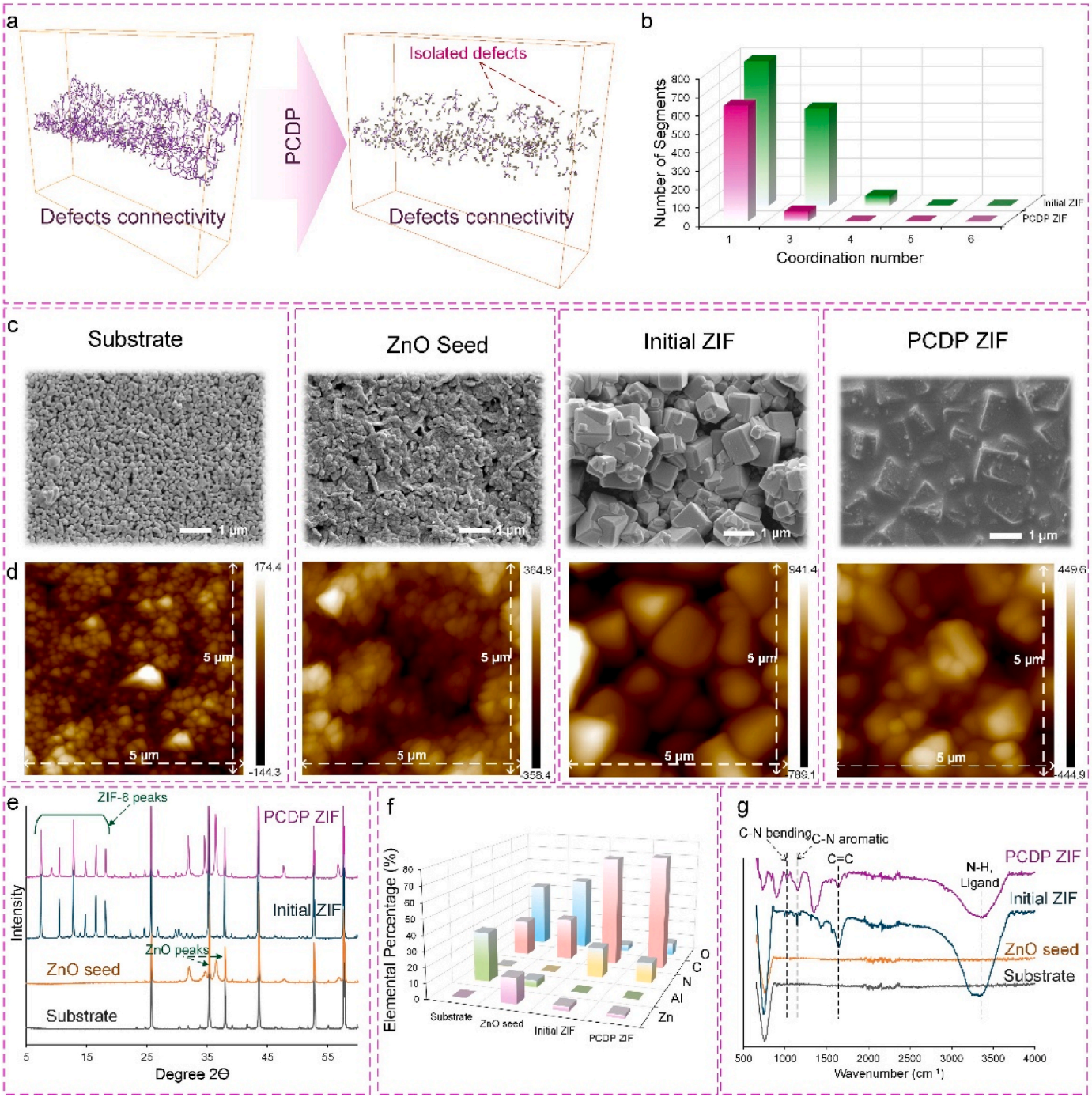

Fig. 2. Further analysis results on membrane morphology and compositions. (a) Defects connectivity using FIB-SEM for the initial ZIF and the PCDP ZIF, (b) the coordination number of defects segments in the initial ZIF and the PCDP ZIF (c) Surface SEM images (d) AFM surface topology images and roughness (e) XRD pattern and crystallinity peaks between 5° and 60° and with 0.5°/min time per step, (f) XPS elemental percentage for Zn2p, Al2p, N1s, C1s, and O1s, and (g) FTIR spectra of the samples in each fabrication step.

confirming the self-healing capability of this method (Fig. 1f and Fig. S7 and S8).

The resulting ZIF membrane using this technique (named PCDP ZIF) exhibited a significant increase in H_2/N_2 selectivity, accompanied by a reduction in H_2 permeation due to defect and crack filling (Fig. 1g). The H_2/N_2 selectivity increased from 2.5 to 41.3 (more than 16 times higher) after the defect healing process. Additionally, the N_2 permeation in this membrane is two orders of magnitude lower than the initial ZIF, providing evidence for defect sealing and hindrance of N_2 molecules, thereby enhancing the molecular sieving effect. The comparative analysis of the performance of the PCDP ZIF against the initial ZIF and prior research on ZIF-8 indicates a significant enhancement in the membrane performance. The 3D reconstruction of the PCDP ZIF membrane, conducted utilizing focused ion beam scanning electron microscopy (FIB-SEM), revealed the remarkable healing of 91 % of cracks and defects (defect density from 10 % to 0.89 %) after using the PCDP (Fig. 1h, Fig. S9). The significant healing of defects was also confirmed by the Fluorescent Confocal Optical Microscopy (FCOM) test results (Fig. 1i), which enables the scanning of a large membrane area. The intensified bright regions spanning from the top to the bottom part confirm the existence of numerous defects within the initial membrane. Using image analysis, intercrystalline defects and crystalline edges can be observed clearly in the initial ZIF sample. By sealing these defects with PCDP, the transportation of dye molecules was impeded, preventing their diffusion into the underlying layers and even into the larger substrate pores. Consequently, a notable decrease in the bright areas as well as intercrystalline defects is observed in the PCDP ZIF sample, as evidenced in both surface and cross-sectional imagery.

Apart from total defect volume and density, defect connectivity is also important in determining the fluid pathway and final membrane selectivity. Interconnected defects that form unselective pathways through the membrane can greatly reduce selectivity, while isolated defects have a minor impact on membrane performance [33]. To compare defect connectivity in the initial and PCDP ZIF membranes, FIB-SEM 3D reconstruction and image processing were carried out (Fig. 2a). The extracted data revealed defect segments and their coordination numbers, where the coordination number indicates the number of neighboring defects for each segment. Defects with a coordination number of 1 can be considered isolated, unable to create unselective voids across the membrane, and have a negligible impact on membrane selectivity. The defect connectivity (Fig. 2b) results showed that 92 % of the residual defects in the PCDP ZIF had a coordination number of 1. In contrast, in the initial ZIF, 42 % of defect segments exhibited high coordination numbers, which can significantly reduce selectivity.

The changes in morphology and composition at various stages of fabrication are illustrated in Fig. 2c–g. The initial membrane was synthesized through the typical conversion of a ZnO-seeded substrate via a hydrothermal synthesis method, as reported in previous literature. Subsequently, pressurized counter-diffusion was applied using PCDP to reconstruct the membrane's microstructure, reduce defect density, and enhance membrane selectivity. Atomic Force Microscopy (AFM) analysis revealed an increase in substrate roughness following seeding with ZnO particles, with the Ra value rising from 32.5 nm in the substrate to 89.8 nm post-seeding. This augmentation in roughness effectively enhances adhesion between the ZIF layer and substrate, thereby facilitating heterogeneous nucleation. After the formation of the MOF layer via the hydrothermal method, membrane roughness reached Ra 175 nm, indicative of non-uniform particle growth in diverse directions and the manifestation of various defects. After microstructure evolution using PCDP, membrane roughness decreased to Ra 106 nm, suggesting the mitigation of defects and amalgamation of previously formed particles owing to precursor reaction within intercrystalline defects, thereby promoting the formation of a more homogeneous layer.

The XRD results (Fig. 2e) revealed the preservation of crystalline structure in membranes during the membrane reconstruction process, with identical ZIF-8 peaks visible in both initial and PCDP samples. Additionally, the presence of residual ZnO peaks in the ZIF membranes shows the existence of a few ZnO particles within substrate pores. XPS results (Fig. 2f) for both initial and PCDP ZIF exhibited negligible Al peaks, confirming complete substrate coverage with the ZIF layer. However, heightened intensities of Zn and N peaks in PCDP ZIF membranes indicated enhanced MOF formation. Similar results were observed in FTIR analysis (Fig. 2g), with intensified ZIF peaks, such as C–N aromatic at 1162 cm^{-1} and C–N bending at 1021 cm^{-1}, detected in PCDP ZIF.

3.2. Mechanism

3.2.1. Regulating the reaction location

Targeting the intercrystalline defects requires precise regulation of precursor delivery into these defects. However, the capillary pressure within the defects acts as a barrier to precursor diffusion. To overcome the capillary pressure and address this challenge, temperature and pressure should be controlled effectively. These two parameters critically influence the delivery of precursors and the location of crystallization.

As depicted in Fig. 3a, without the application of pressure, the reactants can still diffuse through the large defects; however, they tend to react on the surface of the first layer rather than filling the defects, resulting in a multiple-layered structure with insufficient density and compactness. By applying pressure to both sides of the substrate, the reactants can overcome the capillary pressure within the defects, facilitating reactions in these areas. The computational fluid dynamics (CFD) simulation clarifies the ligand distribution within intercrystalline defects, supporting this phenomenon, as depicted in Fig. 3b. The CFD outcomes of the MOF membrane in the absence of any applied pressure reveal near-zero fluid velocity within the defects, while higher fluid velocity is observed at the top of MOF particles, favorable for the formation of particles on top of the initial layer, as confirmed by the SEM imaging in Fig. 3c. Applying a relatively higher pressure of 8 bar causes a significant enhancement in fluid velocity within the intercrystalline defects, thereby amplifying the likelihood of MOF nucleation within these gaps. Furthermore, since ligands have a larger size compared to metal ions, they are less likely to diffuse into defects. The application of pressure leads to an increased concentration of ligand molecules in the defects, which, in turn, reduces the possibility of lattice defect formation by providing excess ligand molecules in these targeted locations [34].

It is important to note that, even in the PCDP method, the pressure is kept equal on both sides of the membrane. As a result, there is no pressure gradient to drive precursor transport through the membrane, and ion movement occurs primarily due to the concentration gradient. Therefore, the ion transport from one side of the membrane to the other remains similar in both pressurized and non-pressurized processes. The main role of pressure is in aiding membrane reconstruction by creating a local pressure gradient across the surface and within the defects, rather than across the membrane itself.

To explore the impact of pressure on mitigating capillary pressure within intercrystalline defects, an FCOM investigation was undertaken. Three initial ZIF samples, each containing several intercrystalline defects, were immersed in the dye for three days under varying pressure conditions (0, 4 bar, and 8 bar). As depicted in Fig. 3d–f, the intensity of the brightest sections increased proportionally with the elevation of pressure, indicative of a greater extent of dye penetration into the defects. Notably, at a pressure of 8 bar, a uniform golden hue was observed both on the surface and in the cross-sectional analysis, confirming the diffusion of dye into smaller defects that were previously inaccessible under zero-pressure conditions. These results confirm that at 8 bar pressure, smaller defects can be accessed by precursors for crystal growth.

To compare the dye immersion results with PCDP-ZIF, this reconstructed membrane was also immersed in dye for 3 days under 8 bar pressure. The FCOM results (Fig. S10) showed only minor diffusion of

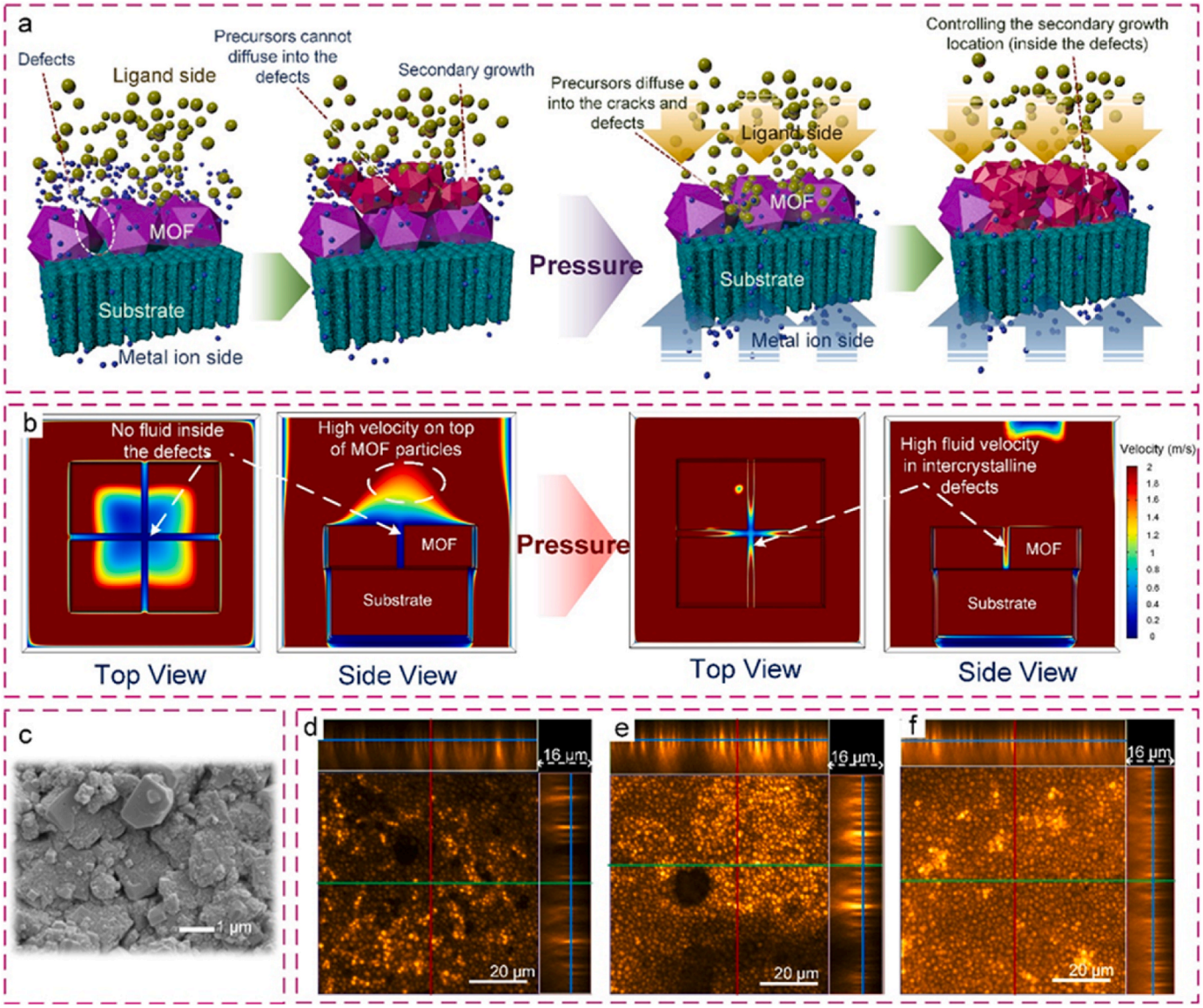

Fig. 3. Regulating the precursor delivery within the intercrystalline defects. (a) The schematic diagram of the pressure effect: the probable reaction of ligand and metal ions at the top of the MOF particles without applying pressure. By applying the desired pressure, the reaction location changes to the ZIF defects. (b) CFD Modeling: The top view and side view of the ligand velocity distribution without applying pressure and after applying pressure. (c) The surface SEM image of the membrane after secondary growth modification (SG-ZIF) in the contra-diffusion cell without applying pressure. (d–f) FCOM test results for initial ZIF soaked in the dye solution under various pressures: d: without pressure, e: 4 bar pressure, f: 8 bar pressure.

dye molecules, confirming substantial sealing of the defects. Based on FCOM analysis and derived compact membrane structure (Fig. 3e, f), a pressure of 8 bar is sufficient for distributing the precursor into small defects for the following crystal growth. However, precursor delivery into all small defects may require significantly higher pressure, necessitating caution at such elevated levels. Excessive pressure can force precursors beyond the primary MOF layer, potentially blocking the substrate pores, as indicated by some crystal growth within the substrate, even at 8 bar. This is supported by the EDX and TEM results of the PCDP ZIF shown in Fig. S11. Therefore, the pressure was not increased further.

The grown ZIF using the non-pressurized PCDP method also improved H_2 selectivity, attributed to the filling of large cracks and defects. This derived membrane also exhibited a 2.8-fold increase in H_2/N_2 selectivity compared to the initial ZIF membrane, but significantly lower than the selectivity of the PCDP ZIF derived from the pressurized PCDP method (Table S3).

Temperature is another crucial parameter that can alter the delivery of precursors. Elevated temperatures enhance both the diffusion rate of precursors and the crystal growth rate. The accelerated diffusion and crystallization of precursors at an elevated temperature of 80 °C result in probable reactions within the substrate pores, as evidenced by the cross-sectional SEM image (Fig. S12). Moreover, the decrease in membrane permeability with lower selectivity compared to room temperature PCDP ZIF confirms that the reaction location has shifted from the MOF layer defects into the substrate pores. Consequently, membranes modified at 80 °C demonstrated 72 % lower permeation and 66 % less selectivity compared to the room temperature PCDP ZIF (Table S3).

3.2.2. Morphology evolution mechanism

A time-dependent study was conducted to better understand the mechanism behind the morphological reconstruction of the ZIF layer using this strategy. It is found that this transformed morphology is driven by the combined effects of these four parameters: 1. ligand and water-induced decomposition under high pressure, 2. Formation of 2D nucleation sites, 3. Overcoming of capillary pressure within defects, and

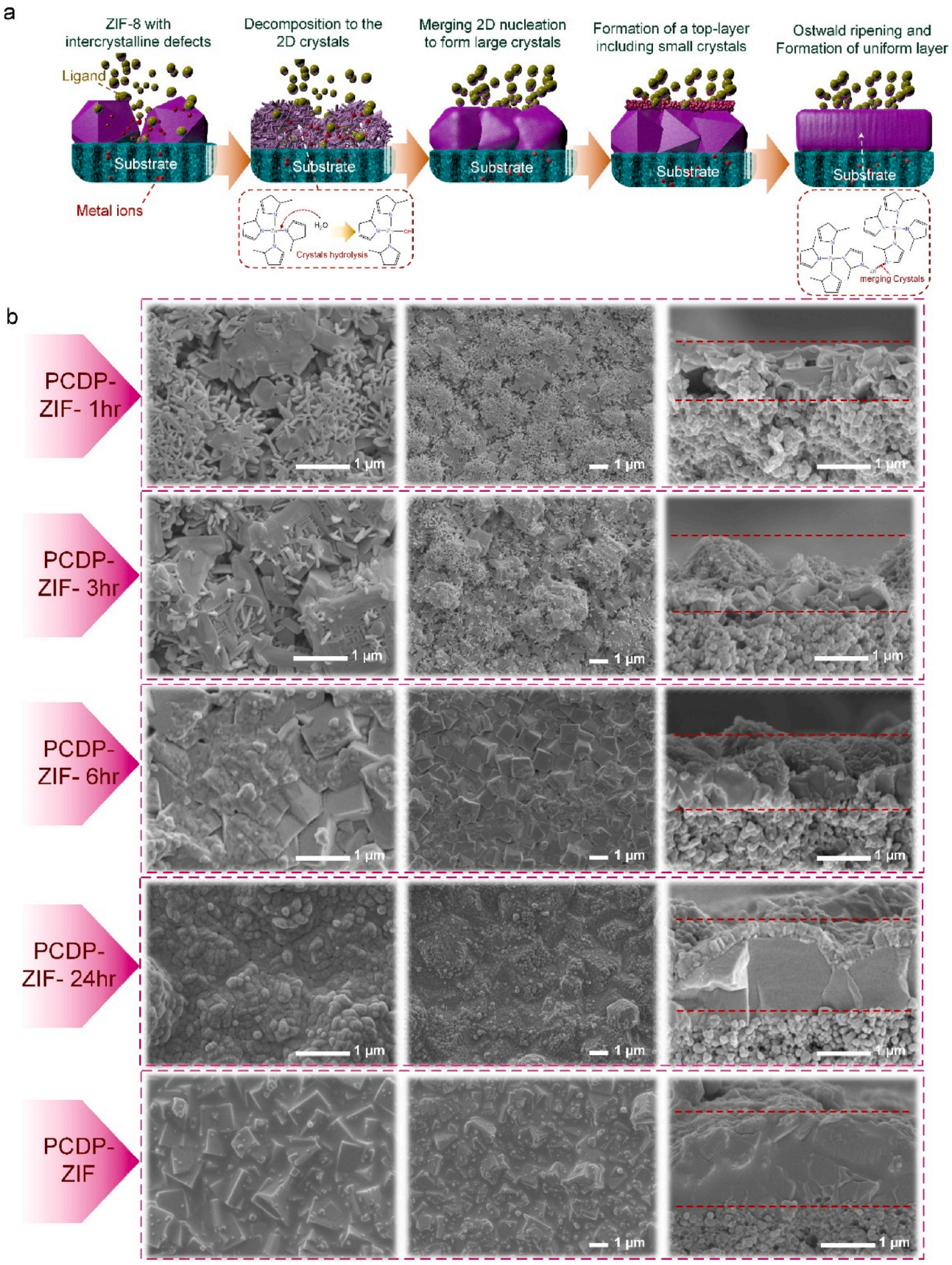

Fig. 4. Microstructure evolution mechanism. (a) The schematic diagram of crystalline evolution during 3 days in PCDP. (b) The Surface and cross-section SEM images of samples during a 3-day reaction time.

4. The Ostwald ripening mechanism (Fig. 4a).

During the first hour of the reaction, the presence of a high concentration of ligand (Hmim) under high pressure leads to the decomposition of the initial ZIF crystals. Hmim in aqueous solution may interact with Zn^{2+} nodes in ZIF-8, weakening the Zn–N coordination bonds and promoting partial dissolution. Additionally, water can break the Zn–N bonds through the hydrolysis process of ZIF-8, contributing to this decomposing mechanism [35]. These unsaturated metal ions have an affinity to coordinate with deprotonated mim-, forming new ZIF-8 nucleation sites. As some Zn^{2+} ions are released from the initial MOF and some others diffuse from the opposite side of the counter cell, their concentration increases, resulting in a high Zn/ligand ratio. This altered Zn/ligand ratio leads to the formation of nanosheets and small 2D ZIF structures as nucleation sites (Fig. 4b- PCDP-ZIF-1hr). On the other hand, the decomposition of the initial ZIF-8 layer begins with the outer crystalline layer and progresses inward, making the diffusion rate of the ligand and water critical. By applying pressure to both sides of the substrate, the mim-/water not only can diffuse deeper and faster into the deeper layers of the initial MOF to recrystallize but also can overcome the capillary pressure within the defects, facilitating reactions in these areas. In the next step, the high surface energy of the small 2D crystals leads to an Ostwald ripening mechanism, where the small particles merge to form larger ZIF-8 particles [36], as evidenced by SEM images of PCDP-ZIF-3hr in Fig. 4b. The recrystallization of ZIF-8 and its merging through Ostwald ripening continues until thermodynamic equilibrium is reached. During this process, the reconstruction of the MOF layer fills and heals most of the large defects and intercrystalline gaps.

After 24 h of reaction, most intercrystalline defects have been sealed, confirmed by the hydrogen selectivity of 25 (Table S3), while still, the top surface of the crystals is under the condition of hydrolysis and nucleation, forming a separate layer of small ZIF-8 crystals (Fig. 4b-(PCDP-ZIF-24hr). Based on the XRD results of PCDP-ZIF-24hr (Fig. S13) and the presence of characteristic ZIF-8 peaks, this top layer can still be identified as ZIF-8 seeds. Gradually, the healed defects block the transportation of Zn^{2+} from the opposite side of the contra cell. In a steady condition after 3 days of reaction, the 200 nm top layer joins the bottom layer in an Ostwald ripening process and results in a uniform ZIF-8 layer with minimum defects.

It is worth mentioning that, in PCDP-ZIF (Fig. 4b-PCDP-ZIF), the intercrystalline pores appear filled with a gel-like or less crystalline material in the SEM images. However, the strong and sharp ZIF-8 peaks in PCDP-ZIF XRD results (Fig. 2e) suggest that the filling material is indeed crystalline ZIF-8. We attribute the gel-like appearance to the slow recrystallization of ZIF-8 from a transient phase, which can form under high ligand concentration and pressure during the PCDP process [37]. This process creates a thin conformal layer that fills grain boundary defects and intercrystalline gaps, leading to a smoother, gel-like morphology on the surface, while maintaining crystallinity in the bulk.

To assess the universality of the PCDP methodology, this strategy has been employed to enhance the properties of the CuBTC membrane. The initial CuBTC membrane was fabricated using $Cu(OH)_2$ seed layer and a solvothermal reaction at room temperature. Similar results have been attained in the PCDP-CuBTC membrane. Conducting the secondary growth in the contra-diffusion apparatus without applying pressure led to the significant filling of large voids and cracks, however, the mitigation of smaller defects was impeded by capillary pressure resistance. Additionally, the deposition of fine particles atop the initial CuBTC layer revealed that after the filling of large cracks, the reaction place changed to the top of the initial layer, not in the defects (Fig. S16b). Conversely, the membrane subjected to PCDP for 3 days at 8 bar pressure exhibited a uniform structure characterized by minimal defects, as depicted in Figure S126c. XRD analyses of the membranes exhibited distinct peaks corresponding to CuBTC both before and after the modification procedures (Fig. S16d). Using the image analysis to quantify the percentage of defects, similar to the PCDP ZIF growth (Fig. S17), the remarkable healing of 98.8 % of cracks and defects (defect density from 24 % to 0.3 %) can be observed after using the PCDP for CuBTC membrane (Fig. S16e).

4. Conclusion

Despite the high potential of molecular sieving membranes in renewable energy and low-carbon footprint technologies, the presence of defects and cracks compromises their performance and scalability. This study introduces a novel pressurized counter-diffusion process (PCDP) for microstructure reconstruction of MOF membranes, effectively addressing the persistent challenge of defects and cracks. By precisely controlling the reaction location, applying high pressure, and inducing recrystallization and microstructure transformation, we achieve a uniform MOF layer with reduced intercrystalline defects. Optimization of key parameters such as temperature, pressure, and precursor concentration facilitated effective morphology transformation, enhancing the separation performance of MOF membranes. The resulting PCDP ZIF membrane demonstrated a remarkable H_2/N_2 selectivity of 41, compared to just 2.5 for the initial ZIF membrane. Additionally, the process successfully sealed 91 % of intercrystalline defects, showcasing its effectiveness. The successful fabrication of a PCDP-CuBTC membrane further underscores the universality and adaptability of this method across various materials. These findings not only deepen our understanding of membrane recrystallization processes but also highlight the potential of PCDP to enhance the selectivity of various MOF and polycrystalline membranes in practical applications.

CRediT authorship contribution statement

Fatereh Dorosti: Writing – review & editing, Writing – original draft, Validation, Methodology, Investigation, Data curation. **Lei Ge:** Writing – review & editing, Writing – original draft, Supervision, Project administration, Methodology, Investigation, Funding acquisition, Formal analysis, Conceptualization. **Shazed Aziz:** Writing – original draft, Formal analysis, Data curation. **John Bell:** Writing – original draft, Resources, Investigation. **Zhonghua Zhu:** Writing – review & editing, Supervision, Resources, Project administration, Methodology, Investigation, Funding acquisition, Conceptualization.

Declaration of competing interest

The authors declare that they have no known competing financial interests or personal relationships that could have appeared to influence the work reported in this paper.

Acknowledgment

Fatereh Dorosti would like to thank the international research scholarship from the University of Queensland. ZH Zhu would like to thank the financial support from the Australian Research Council Discovery Project DP200101397 and the Centre of Excellence for Green Electrochemical Transformation of Carbon Dioxide (CE230100017). L Ge wants to thank the financial support from the ARC Future Fellowship project FT220100166.

Appendix A. Supplementary data

Supplementary data to this article can be found online at https://doi.org/10.1016/j.memsci.2025.124606.

Data availability

All data supporting the findings of this study are included within the article and its Supplementary Information.

References

[1] P. Stanley, V. Ramm, R. Fischer, J. Warnan, Analysis of metal–organic framework-based photosynthetic CO2 reduction, Nature Synthesis 3 (2024) 307–318.
[2] Q. Qian, P.A. Asinger, M.J. Lee, G. Han, K. Mizrahi Rodriguez, S. Lin, et al., MOF-based membranes for gas separations, Chem. Rev. 120 (2020) 8161–8266.
[3] Q. Ma, T. Zhang, B. Wang, Shaping of metal-organic frameworks, a critical step toward industrial applications, Matter 5 (2022) 1070–1091.
[4] F. Dorosti, L. Ge, H. Wang, Z. Zhu, A path forward: understanding and mitigating defects in polycrystalline membranes, Prog. Mater. Sci. (2023) 101123.
[5] G. Liu, C. Chen, B. Mo, G. Zhou, J. Li, Y. Zhang, et al., Angstrom-scale defect-free crystalline membrane for sieving small organic molecules, Adv. Mater. (2024) 2416669.
[6] J. Yao, D. Dong, D. Li, L. He, G. Xu, H. Wang, Contra-diffusion synthesis of ZIF-8 films on a polymer substrate, Chem. Commun. 47 (2011) 2559–2561.
[7] X. Ma, Y. Li, A. Huang, Synthesis of nano-sheets seeds for secondary growth of highly hydrogen permselective ZIF-95 membranes, J. Membr. Sci. 597 (2020) 117629.
[8] G. Yu, X. Shangguan, Z. Wang, H. Rong, K. Wang, Y. Zhang, et al., Seed assisted synthesis of an anionic metal–organic framework membrane for selective and permeable hydrogen separation, Inorg. Chem. Front. 9 (2022) 1636–1643.
[9] C. Yu, Y. jae Kim, J. Kim, M. Hayashi, D.W. Kim, H.T. Kwon, et al., A sacrificial ZIF-L seed layer for sub-100 nm thin propylene-selective ZIF-8 membranes, J. Mater. Chem. A 10 (2022) 15390–15394.
[10] B. Wang, Wt Zhao, X. Xu, C. Zhang, Sy Ding, Y. Zhang, et al., Binary-cooperative ultrathin porous membrane for gas separation, Adv. Mater. 36 (2024) 2309572.
[11] S. Guthrie, L. Huelsenbeck, A. Salahi, W. Varhue, N. Smith, X. Yu, et al., Crystallization of high aspect ratio HKUST-1 thin films in nanoconfined channels for selective small molecule uptake, Nanoscale Adv. 1 (2019) 2946–2952.
[12] J.-C. Lee, J.-O. Kim, H.-J. Lee, B. Shin, S. Park, Meniscus-guided control of supersaturation for the crystallization of high quality metal organic framework thin films, Chem. Mater. 31 (2019) 7377–7385.
[13] X. Zhang, Y. Li, C. Van Goethem, K. Wan, W. Zhang, J. Luo, et al., Electrochemically assisted interfacial growth of MOF membranes, Matter 1 (2019) 1285–1292.
[14] S. Hong, D. Kim, Y. Jeong, E. Kim, J.C. Jung, N. Choi, et al., Healing of microdefects in SSZ-13 membranes via filling with dye molecules and its effect on dry and wet CO2 separations, Chem. Mater. 30 (2018) 3346–3358.
[15] L. Sheng, C. Wang, F. Yang, L. Xiang, X. Huang, J. Yu, et al., Enhanced C 3 H 6/C 3 H 8 separation performance on MOF membranes through blocking defects and hindering framework flexibility by silicone rubber coating, Chem. Commun. 53 (2017) 7760–7763.
[16] D. Korelskiy, P. Ye, M.S. Nabavi, J. Hedlund, Selective blocking of grain boundary defects in high-flux zeolite membranes by coking, J. Mater. Chem. A 5 (2017) 7295–7299.
[17] Y. Yan, M.E. Davis, G.R. Gavalas, Preparation of highly selective zeolite ZSM-5 membranes by a post-synthetic coking treatment, J. Membr. Sci. 123 (1997) 95–103.
[18] Z.Y. Yeo, S.-P. Chai, P.W. Zhu, A.R. Mohamed, An overview: synthesis of thin films/membranes of metal organic frameworks and its gas separation performances, RSC Adv. 4 (2014) 54322–54334.
[19] S. Jiang, X. Shi, Y. Zu, F. Sun, G. Zhu, Interfacial growth of 2D MOF membranes via contra-diffusion for CO 2 separation, Mater. Chem. Front. 5 (2021) 5150–5157.
[20] J.H. Lee, D. Kim, H. Shin, S.J. Yoo, H.T. Kwon, J. Kim, Zeolitic imidazolate framework ZIF-8 films by ZnO to ZIF-8 conversion and their usage as seed layers for propylene-selective ZIF-8 membranes, J. Ind. Eng. Chem. 72 (2019) 374–379.
[21] X. Wang, M. Sun, B. Meng, X. Tan, J. Liu, S. Wang, et al., Formation of continuous and highly permeable ZIF-8 membranes on porous alumina and zinc oxide hollow fibers, Chem. Commun. 52 (2016) 13448–13451.
[22] A. Ronte, P. Wagle, G. Mahmodi, M. Chevula, S. Dangwal, M.R. Saeb, et al., High-flux ZIF-8 membranes on ZnO-coated supports for propane/propylene separation, Energy Fuels 37 (2023) 8456–8464.
[23] J. Yu, Y. Pan, C. Wang, Z. Lai, ZIF-8 membranes with improved reproducibility fabricated from sputter-coated ZnO/alumina supports, Chem. Eng. Sci. 141 (2016) 119–124.
[24] W. Li, J. Shi, Z. Li, W. Wu, Y. Xia, Y. Yu, et al., Hydrothermally reduced graphene oxide interfaces for synthesizing high-performance metal–organic framework hollow fiber membranes, Adv. Mater. Interfac. 5 (2018) 1800032.
[25] Y. Li, C. Ma, P. Nian, H. Liu, X. Zhang, Green synthesis of ZIF-8 tubular membranes from a recyclable 2-methylimidazole water-solvent solution by ZnO nanorods self-converted strategy for gas separation, J. Membr. Sci. 581 (2019) 344–354.
[26] S. Zhang, Z. Wang, H. Ren, F. Zhang, J. Jin, Nanoporous film-mediated growth of ultrathin and continuous metal–organic framework membranes for high-performance hydrogen separation, J. Mater. Chem. A 5 (2017) 1962–1966.
[27] S. Tanaka, K. Okubo, K. Kida, M. Sugita, T. Takewaki, Grain size control of ZIF-8 membranes by seeding-free aqueous synthesis and their performances in propylene/propane separation, J. Membr. Sci. 544 (2017) 306–311.
[28] X. Jiang, S. Li, Y. Bai, L. Shao, Ultra-facile aqueous synthesis of nanoporous zeolitic imidazolate framework membranes for hydrogen purification and olefin/paraffin separation, J. Mater. Chem. A 7 (2019) 10898–10904.
[29] Y. Wang, H. Zhang, X. Wang, C. Zou, B. Meng, X. Tan, Growth of ZIF-8 membranes on ceramic hollow fibers by conversion of zinc oxide particles, Ind. Eng. Chem. Res. 58 (2019) 19511–19518.
[30] Y. Qin, L. Xu, L. Liu, Z. Ding, Zeolitic imidazolate framework membranes with a high H2 permeance fabricated on a macroporous support with novel spherical porous hybrid materials, Ind. Eng. Chem. Res. 60 (2021) 1387–1395.
[31] Y. Wang, H. Chen, X. Wang, B. Meng, N. Yang, X. Tan, et al., Preparation of ZIF-8 membranes on porous ZnO hollow fibers by a facile ZnO-induced method, Ind. Eng. Chem. Res. 59 (2020) 15576–15585.
[32] P. Yang, Z. Li, Z. Gao, M. Song, J. Zhou, Q. Fang, et al., Solvent-free crystallization of zeolitic imidazolate framework membrane via layer-by-layer deposition, ACS Sustain. Chem. Eng. 7 (2019) 4158–4164.
[33] W. Ding, H. Li, P. Pfeifer, R. Dittmeyer, Crystallite-pore network model of transport and reaction of multicomponent gas mixtures in polycrystalline microporous media, Chem. Eng. J. 254 (2014) 545–558.
[34] G. Liu, Y. Guo, C. Chen, Y. Lu, G. Chen, G. Liu, et al., Eliminating lattice defects in metal–organic framework molecular-sieving membranes, Nat. Mater. (2023) 1–8.
[35] H. Zhang, M. Zhao, Y. Yang, Y. Lin, Hydrolysis and condensation of ZIF-8 in water, Microporous Mesoporous Mater. 288 (2019) 109568.
[36] Z. Zou, Z. Du, L. Dai, D. Liu, W. Du, Crystallization mechanisms and size control of metal-organic frameworks: insights and applications, Chem. Eng. J. 480 (2024) 148260.
[37] J.A. Allegretto, D. Onna, S.A. Bilmes, O. Azzaroni, M. Rafti, Unified roadmap for ZIF-8 nucleation and growth: machine learning analysis of synthetic variables and their impact on particle size and morphology, Chem. Mater. 36 (2024) 5814–5825.